

Peer Reviewed Paper openaccess

# Development of a multispectral microscopy platform using laser diode illumination for effective and automatic label-free *Plasmodium falciparum* detection

Yao T. Alvarez Kossonou\* and Jérémie T. Zoueu

Laboratoire d'Instrumentation, Image et Spectroscopie (L2IS), Institut National Polytechnique - Felix Houphouët Boigny, BP 1093 Yamoussoukro, Côte d'Ivoire

## Contact

Yao Alvarez Kossonou: [takyalvarez79@gmail.com](mailto:takyalvarez79@gmail.com);  
<https://orcid.org/0000-0001-9807-3846>

Jérémie Zoueu: [jeremie.zoueu@inphb.edu.ci](mailto:jeremie.zoueu@inphb.edu.ci);  
<https://orcid.org/0000-0003-4588-1641>

In this paper, we present the progress made in developing multimodal and multispectral light microscopy for label-free malaria diagnosis. Our previously developed light emitting diode (LED) illumination system was replaced by laser diodes as light sources in order to narrow the spectral bands and improve the effectiveness of the contrast function for infected blood cell detection. The acquisition system is now equipped with an algorithm for automatic field scanning and best in-focus determination. We demonstrate the potential of this platform to provide multiple investigation modalities like transmission, reflection, scattering, fluorescence, excitation, emission and polarisation. The application of this platform on malaria-infected samples has shown the effectiveness of such a system in label-free and all-optical malaria detection by allowing the possibility of using a different type of imaging set-up for the samples analysed. Also, fewer illumination sources are used to characterise malaria-infected red blood cells compared to our previous works on malaria detection using LEDs illumination sources.

**Keywords:** multispectral imaging microscopy, motorised microscope, autofocus algorithm, imaging modalities, biological diagnosis

## Introduction

The use of hyperspectral and multispectral imaging techniques in remote sensing imagery, cultural heritage conservation, biomedical and agriculture studies have been demonstrated to be powerful investigation methods. An increasing number of studies are related to the development of analytical tools based on the combination of imaging and spectroscopy techniques.<sup>1-3</sup> New types of optical microscopes have thus been developed

including multispectral optical microscopes based on light emitting diodes (LEDs)<sup>4-6</sup> which were widely used for their simplicity.

The development of optical and electronic components such as complementary metal-oxide-semiconductor (CMOS) imagers, light-emitting diodes, lasers etc. has enabled the construction of affordable tools for scientific research.<sup>7-9</sup> From a modified Brunel Compound

### Correspondence

Yao Alvarez Kossonou ([takyalvarez79@gmail.com](mailto:takyalvarez79@gmail.com))

**Received:** 6 July 2020

**Revised:** 28 October 2020

**Accepted:** 8 December 2020

**Publication:** 21 December 2020

**doi:** 10.1255/jsi.2020.a17

**ISSN:** 2040-4565

### Citation

Y.T. Alvarez Kossonou and J.T. Zoueu, "Development of a multispectral microscopy platform using laser diode illumination for effective and automatic label-free *Plasmodium falciparum* detection", *J. Spectral Imaging* 9, a17 (2020). <https://doi.org/10.1255/jsi.2020.a17>

© 2020 The Authors

This licence permits you to use, share, copy and redistribute the paper in any medium or any format provided that a full citation to the original paper in this journal is given, the use is not for commercial purposes and the paper is not changed in any way.



microscope,<sup>10,11</sup> we built a low-cost multispectral optical microscope. It was designed to enable image acquisition with more than three spectral bands. Equipped with 13 LEDs ranging from 370 nm to 940 nm, it has three imaging modalities (transmission, reflection and scattering). On the same scene of the sample and for each LED, an image is captured using a 12-bit pixel depth monochrome CMOS camera of 5 MP (2592 × 1944, Guppy-503B, Allied Vision Technology containing a MT9P031 sensor from Micron/Alpha). This system was utilised as an alternative tool for staining-free malaria diagnosis.<sup>12–14</sup> The same instrument was also used to study, analyse, predict and build statistical models of infected tropical plant leaves<sup>15–17</sup> to enhance agricultural production. The potential of this optical microscope to spectrally differentiate and classify the samples' content also made it a valuable tool for biological diagnostic approaches.<sup>18</sup> Multispectral imagery provides more meaningful information than a single image for biological cell analysis and has proven to be more effective for characterising complex samples.<sup>19,20</sup>

Despite the important results achieved over the past years using the multispectral and multimodal microscope utilising LEDs (375–940 nm) as previously presented,<sup>14</sup> a number of limitations were found in the system performance: the spectral bandwidth of a LED is not narrow enough to build an effective contrast function using spectroscopic markers for biomedical diagnostics; quantitative characterisation and classification of biological samples require more accuracy when using spectral fingerprints. A number of studies require the storage of the image acquisition parameters for their reuse; this was not possible using a manual positioning system, which is in addition time consuming for non-expert users. Furthermore, routine examination of thick and thin blood films for accurate malaria detection requires the scanning of at least 100 good fields.<sup>21</sup> Since the LED microscope was built using a commercial metallurgical system designed for transmission, reflection and scattering modes, the implementation of additional modalities or illumination sources was limited.

The construction of this new multispectral and multimodal microscope aims to address the limitations cited above and allows investigation involving several microscope configurations such as transmission, reflection, excitation, fluorescence, polarisation, defocus, diffraction, interference and super resolution,<sup>22–24</sup> in addition to being cost-effective with the ability to evolve in space and time according to the needs of the user by adding new optical components (such as optical densities, polarisers,

optical filters, new illuminations sources and optical lens) without modifying the default system path.

The paper is structured as follows: the Introduction presents the motivation and objectives of this work. Materials and methods presents the optical and electronic components used to build the microscope and the algorithm discussion for focal plane settings. Results and discussion shows how the proposed new optical system has improved label-free malaria detection.

## Materials and methods

### Materials

The proposed optical microscope can be divided in four main parts: the optical and mechanical components, the illumination sources, the automated stage and the electronic system. We chose to assemble the proposed instrument from both commercial and home-built parts in order to make it more flexible and ease the integration of new components and/or configurations. The default system configuration consists of an arrangement of optical, mechanical and electronic components presented in Figure 1.

The system is equipped with a Lumenera It225M camera that has 5.5 × 5.5 μm pixel size. It utilises USB 3.0 technology with selectable 12- or 16-bit pixel data with a high-resolution 2/3" CMOSIS CMV2000 sensor and a fully electronic global shutter. This is a fast camera using a sensor with a resolution up to 2.2 MP (1088 × 2048) and a maximum frame of 170 fps (frame per second). Its exposure time ranged from 0 s to 4 s and gain from 1 to 40, revealing its high sensitivity. The size of imaged objects depends on replaceable optical objectives, including Olympus Nikon NEOFLUAR 6.3/0.2, 40/0.7 and 100/1.25. A cassegrain objective is alternatively used<sup>11</sup> in order to overcome the chromatic aberration. This reflective objective has a numerical aperture of 0.28, a focal length of 13.3 mm and a working distance of 23.75 mm. The set of laser sources consists of six wavelengths (405 nm, 450 nm, 532 nm, 638 nm, 660 nm and 850 nm). It can be alternatively replaced by a set of LEDs. The default geometrical configuration of the system consists of transmission and reflection modes. The number of illumination sources can be modified without changing the optical path of the experimental setup. Switching automatically from one mode to another and one wavelength to another is made possible by the use of a data acquisition card (DAQ) from National Instruments (USB 6008). Optical fibres are used to direct

light beams toward the main optical system which pass through a speckle reducer (Optotune Laser speckle reducer, Edmund Optics) to lower the speckle noise, followed by various neutral density filters<sup>25</sup> to control the light intensity.

Thanks to the versatility of the optical design, the system can be used for various applications as both a malaria diagnosis tool<sup>26,27</sup> and an investigation platform for plant leaf health.<sup>28</sup> New experimentation is achieved by inserting extra components corresponding to the desired set-up. For example, fluorescence experiments were performed by inserting a set of spectral filters (FEL405 to FEL700, Thorlabs) between the camera and the optical objective. Polarisation microscopy was implemented by using two mounted polarisers from Thorlabs (LPV series).

Images from optical microscopy may suffer from various limitations such as blurring, over or under exposure, non-uniform illumination and out-of-focus effects.<sup>29</sup> To address the risk of potential defocus blur, the system is equipped with three motors from Thorlabs. These motors are controlled using TDC001 servo-controllers. The motors used are characterised by a shaft-distance dimension of 25 mm (0–25 mm) and a

minimum step length of 0.5  $\mu\text{m}$ . The servo-controllers are used to move the sample in three directions, namely x, y and z-axes.

Several regions of interest (ROI) of the sample can be explored using the x- and y-axis automatic control capability, adding interest to experiments such malaria diagnosis for which, the accuracy of parasite detection increases with the number of scanned ROIs. The capability of analysing different ROIs increases the system effectiveness because it allows the user search infection on different areas of the sample. This increases the probability of infection detection. The whole system is controlled by Matlab (2014a release) code with a Graphical User Interface (GUI).

The GUI controls the exposure time, gain, automatic switching between illumination sources and the best-in-focus image finding. The image backup files contain the factors outlined above. The graphical interface shows a live preview picture of the sample, the pixels' standard deviation value, the number of saturated pixels and the histogram of the current displayed frame.

Focus setting is done along the z-axis and depends on the images content. Several authors have proposed methods for the best in-focus point image from a set

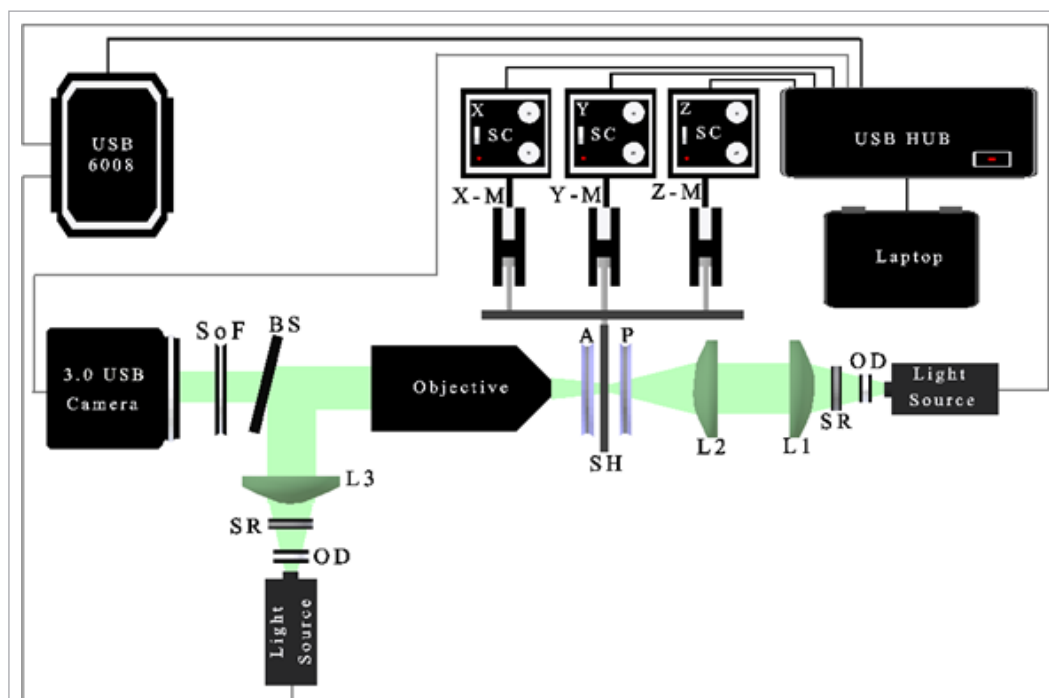


Figure 1. Schematic of the proposed system where OD and SR represent, respectively, the optical density and speckle reducer. L, P and A are the lens, polariser and the analyser. The sample holder, beam splitter and set of filters ranging from 405 nm to 700 nm are described as SH, BS and SoF. X-M, Y-M and Z-M stand for the motor control following x-axis, y-axis and z-axis. X SC for the servo-controller controlling x-motor, Y SC for the servo-controller managing y-motor and Z SC means the servo-controller monitoring the z-motor.

of captured microscopic images.<sup>29</sup> In what follows, we summarise one of these autofocus algorithms. The best algorithm performance in terms of speed corresponds to the one-dimensional Fourier transform defined by:

$$H(f) = \int_{-\infty}^{+\infty} h(x) \exp(-j2\pi fx) dx \quad (1)$$

After applying the above formula, a correlation coefficient defined by Pearson is used to get the likeness rate of a couple of images. It is computed as follows:

$$r = \frac{\sum XY - \frac{\sum X \sum Y}{\zeta}}{\left\{ \left[ \sum X^2 - \frac{(\sum X)^2}{\zeta} \right] \left[ \sum Y^2 - \frac{(\sum Y)^2}{\zeta} \right] \right\}^{1/2}} \quad (2)$$

The paper<sup>29</sup> also includes Tenenbaum's Algorithm (SOB-TEN), Boddeke's Algorithm (BOD), Laplacian gradient Magnitude variance (SOB VAR) etc. These algorithms perform very well but still have a long execution time.

In the next section, we present our algorithmic approach to determine the best in-focus image using a simple formula. This algorithm is rapid and accurate for auto-focus. The proposed method is based on the standard deviation of the approximate derivative of the image.

## Methods

This part describes the proposed method to set the best focus plane. We are interested in biological samples with flat edges. By default, the z-axis ranges from 0mm to 25mm. The finding of the best in-focus image is based on the use of the standard deviation of the approximate derivative (STD\_DER) applied to images acquired on the full range of z-axis (0–25mm). Prior to this, the images are normalised and preprocessed to remove artefacts. Image normalisation is a process applied to the input images. After application, the output image pixels intensity is between 0 and 1. The preprocessing step is useful in the case of blurred and noisy images. It improves the differentiation of the objects from the background. The software enables the user to choose the scanning range by fixing the desired extreme values to find the best in-focus image. Practically, an image is taken at each step. The step is defined as:

$$Step = \frac{Max_V - Min_V}{N_p} \quad (3)$$

with  $Max_V$ ,  $Min_V$  and  $N_p$ , respectively, standing for maximum value, minimum value and number of planes to

scan. By default, the number of planes to scan is 20 and can be edited by the user. To quickly find the in-focus range, we use the maximum of the difference between the standard deviation of the current image and the nearest one.

If  $x_{ij}$  is the pixel intensity of an image, its standard deviation is defined by:

$$standard\_deviation = \sqrt{\frac{1}{M \times N} \sum_{i=1}^M \sum_{j=1}^N (x_{ij} - \mu)^2} \quad (4)$$

while

$$\mu = \frac{\sum_{i=1}^M \sum_{j=1}^N x_{ij}}{M \times N} \quad (5)$$

with  $M$  the number of rows in the image and  $N$  the number of columns;  $i$  denotes the image rows index and  $j$  the columns index. Let us assume  $standard\_deviation\_1$  and  $standard\_deviation\_2$ , the standard deviations taken at two consecutive positions position1 and position2, respectively. Then, the in-focus point will be at:

$$\begin{cases} \text{position1} \\ \text{if } \left( \begin{matrix} standard\_deviation\_1 \\ standard\_deviation\_2 \end{matrix} - \right) < 0 \\ \text{position 2 else} \end{cases} \quad (6)$$

This method is applied to the full range. This process is fast because of the speed of standard deviation computation. To get the position at which the best in-focus image is, we use the following step which is applied to each acquired image in the reduced range. The approach based on the approximate image derivatives was inspired by the one named LAP\_VAR, SOB-TEN, LAP, BOD.<sup>29</sup> These methods perform first and second derivatives on the images. They work well, but are time consuming. Whilst we use the computation of the image second derivative, we also propose a much faster approximation. The derivative of an image tells us how smooth it is. Simply, this derivative estimates the difference between a point and another along the rows or columns. Let  $X(i,j)$  be the matrix associated with an acquired image. After applying the approximate derivative to columns of this matrix, the pixel value located at  $(i,j)$  position will be replaced as follows:

$$Result\_Column(i,j) = [x(i,j+1) - x(i,j)] - [x(i,j+2) - x(i,j+1)] \quad (7)$$

If  $M$  is the number of rows of the matrix and  $N$  the number of columns, the result matrix will have  $M$  rows

and  $(N - 2)$  columns. Nonetheless, this operation can be performed on the rows instead of columns. In that case, the pixel value located at  $(i, j)$  position becomes:

$$\text{Result\_Row}(i, j) = [x(i, j) - x(i + 1, j)] - [x(i + 1, j) - x(i + 2, j)] \quad (8)$$

$$\text{Result\_Row}(i, j) = [x(i, j) - 2 \times x(i + 1, j)] + x(i + 2, j) \quad (9)$$

In that case, the result matrix will have  $(M - 2)$  rows and  $N$  columns. Then, to remove the dependence of rows or columns the final result is given as:

$$\text{Final}_{\text{Result}} = \sqrt{\text{Result\_Row}^2 + \text{Result\_Column}^2} \quad (10)$$

The algorithm used is summarised in Figure 2 and comprises four main steps: the preprocessing part to improve image quality, the retrieving of the in-focus range to reduce the algorithm processing time, the application of standard deviation of approximate derivative on the in-focus range to get the best in-focus distance and the finding of the best in-focus plane using the third step.

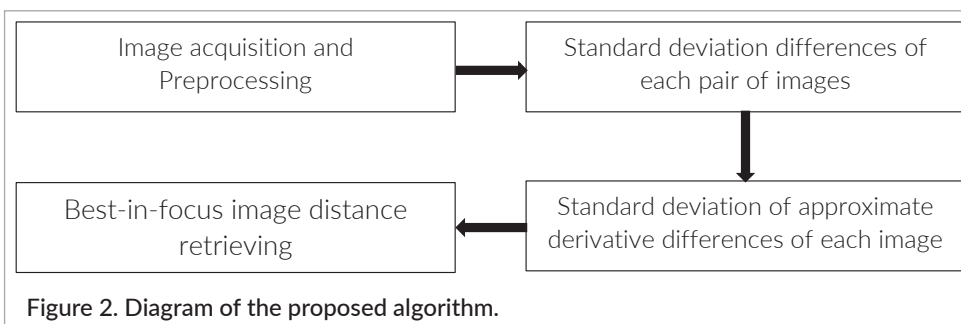
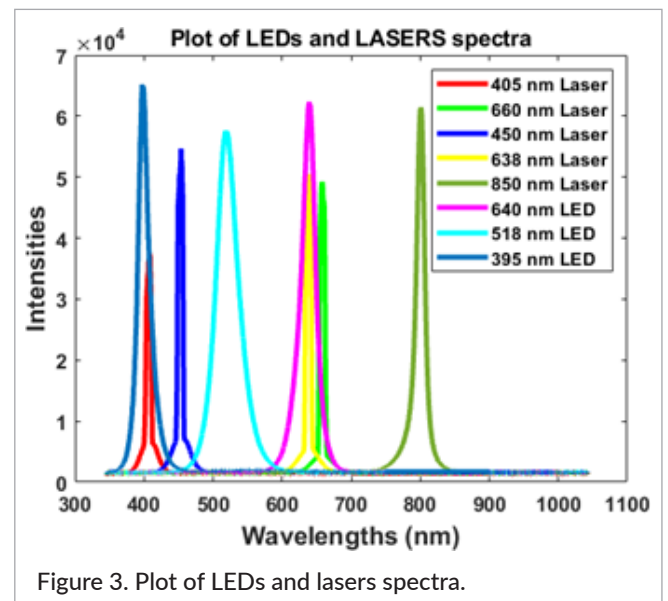
The system using lasers as illumination sources, previously described, was applied to red blood samples. The ones used in our work were acquired from human red blood cells. Samples were collected from the fingers of malaria-infected patients. Next, these are spread on corrosion-resistant glasses from CITOPLUS REF 0303-0004. Then, they are dried in a closed environment to avoid contamination, such as dust, for 7–15 min each. The samples were not stained to preserve the optical properties of the blood cells. Then, they were imaged using the multispectral and multimodal microscope.

## Results and discussion

Our previous optical system<sup>10–11</sup> was upgraded from LED illumination to laser sources to narrow the light spectral bandwidth. Figure 3 compares both LEDs and laser illumination sources spectral bands. The spectra were

recorded using an Ocean Optics USB4000-FL spectrometer (2008 series) and show narrower half bandwidths for laser illumination. The choice of wavelengths from lasers sources in this work has been made according to the need to undertake malaria diagnosis. When infected, haemoglobin, being the main constituent of red blood cells, presents absorption peaks around 405 nm, 532 nm and 660 nm. Infected as well as uninfected red blood cells show the highest absorption around 405 nm.<sup>10–14</sup> The absorbance of infected red blood cells in the spectral range 625–700 nm is higher than that in the range 470–590 nm.<sup>30</sup> This reduction can be explained by the presence of malaria infection. The knowledge of this information is relevant to propose a contrast function as described below.

As mentioned, this study comprises two major parts. First, we describe the design and performance of a new laser-based multispectral and versatile optical microscope, with the proposed autofocus algorithm, followed by some results. The automatic focal plane detection is obtained thanks to the algorithm described above. We evaluate the performance of the code by acquiring a set



of images along the z-axis, and using both visual inspection and standard deviation as references to estimate in-focus sample accuracy.

We also compare the execution time and the focal plane setting factors of the proposed algorithm to a set of existing algorithms.<sup>29</sup> Of the many existing codes tested, "One Dimensional Fourier Transform and Pearson Correlation (P.CORR)" gives a comparative performance in terms of execution time. The run-time efficiency similarity of both P.CORR and the proposed new algorithm (STD\_DER) can be seen in Table 1. However, for large images our code achieves better results. The other tested algorithms result in longer run-times.

Next, the focal plane setting indices are compared for both P.CORR and STD\_DER. Different images of regions of interest were screened.

The number of images to scan depends on many parameters that must be set by the user: the number of images to scan or the resolution step, meaning the distance between two images taken at different positions, the maximum and the minimum distance of the Z-motor. The maximum and the minimum distance denote the autofocus range finding. Mathematically, the number of images can be calculated using Equation (3). In that equation, the number of plans to scan denoted by  $N_p$  corresponds to the number of images.

The results in Table 2 proves that the proposed new algorithm is faster. Figure 4 shows some of the best in-focus images obtained with the various algorithms. It

presents the best in-focus images for various condenser positions. Some contrast variations can be seen from one position to another. The parameter for finding the best in-focus image is based on a simple equation: standard deviation of the approximate derivative of the image (STD\_DER). Figure 4 shows images which can be seen as best in-focus images. They are very similar in terms of border sharpness except the first which is a little blurred.

The system has been used for different types of modalities like transmission, reflection, fluorescence and polarisation. For fluorescence, the excitation line was at 405 nm and the emission was filtered using a long-pass edge filter with a cut-off at 450 nm. First, the focal plane was located, then a long-pass filter (SoF in Figure 1) was used.

The four following Malaria Infection Indices (MII), expressed by Equations (11) to (14), have been proposed and tested on four spectral images captured using 532 nm, 638 nm, 532 nm and 650 nm from red blood samples:

$$MII1 = [\log(R532nm) - \log(T638nm)] / [\log(R532nm) + \log(T638nm)] \quad (11)$$

$$MII2 = (R532nm - T638nm) / (R532nm + T638nm) \quad (12)$$

$$MII3 = [\log(T405nm) - \log(R650nm)] / [\log(T405nm) + \log(R650nm)] \quad (13)$$

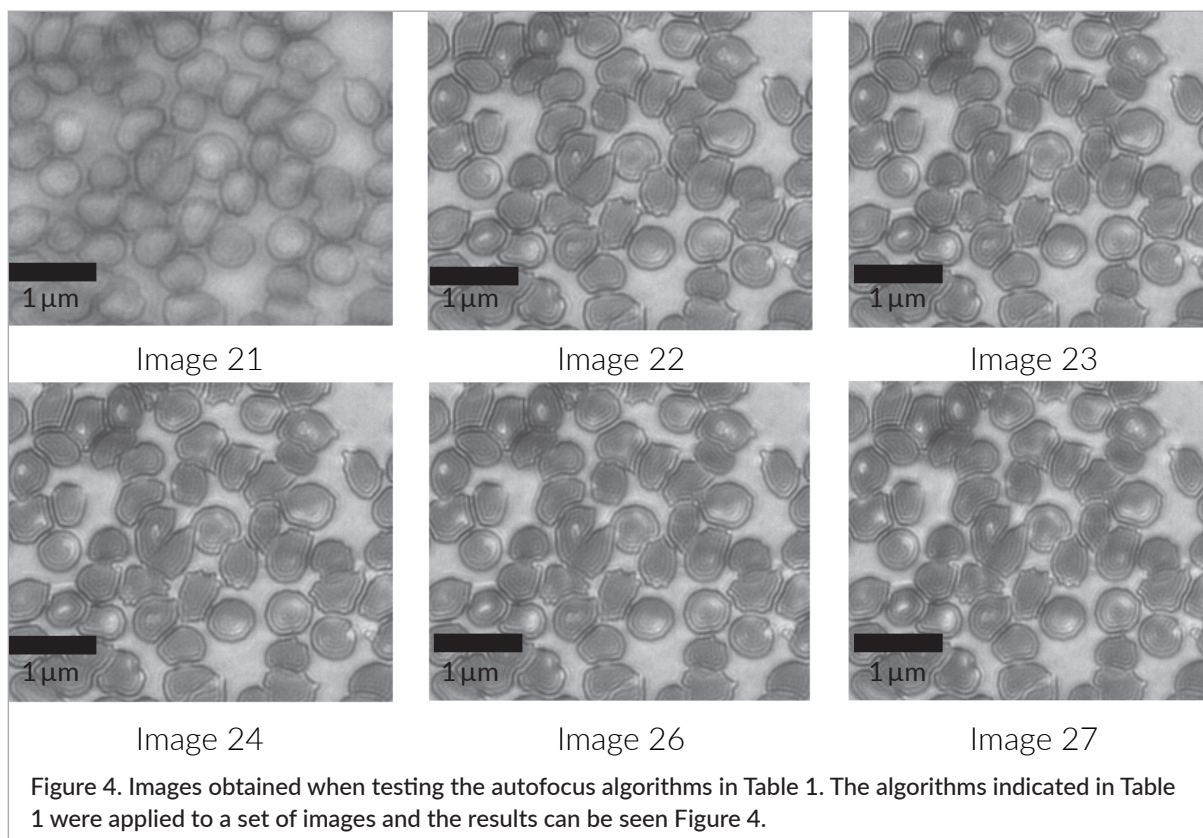
$$MII4 = (T405nm - R650nm) / (T405nm + R650nm) \quad (14)$$

Table 1. Autofocus time of tested algorithms.

| Image size           | 544 × 664   |                    | 677 × 1115  |                    | 1069 × 1662 |                    | 1088 × 2048 |                    |
|----------------------|-------------|--------------------|-------------|--------------------|-------------|--------------------|-------------|--------------------|
| Algorithms           | Image index | Execution time (s) |
| SOB-TEN              | 22          | 271.469            | 22          | 660.623            | 22          | 1084.971           | 22          | 1565.853           |
| LAP                  | 22          | 107.423            | 22          | 228.273            | 22          | 523.744            | 22          | 983.820            |
| LAP-VAR              | 22          | 190.699            | 22          | 372.166            | 22          | 1062.523           | 22          | 1836.500           |
| P.CORR               | 22          | 06.387             | 22          | 08.87              | 22          | 21.064             | 22          | 26.34              |
| STD_DER (this study) | 22          | 06.156             | 22          | 08.51              | 22          | 16.855             | 22          | 22.0733            |

Table 2. Accuracy and execution time of P.CORR and STD\_DER.

| Image size           | 44 × 52     |                    | 52 × 62     |                    | 111 × 165   |                    | 152 × 380   |                   |
|----------------------|-------------|--------------------|-------------|--------------------|-------------|--------------------|-------------|-------------------|
| Algorithms           | Image index | Execution time (s) | Image index | Execution time (s) | Image index | Execution time (s) | Image index | Execution time(s) |
| P.CORR               | 23          | 2.441              | 23          | 2.486              | 23          | 2.727              | 21          | 2.97              |
| STD_DER (this study) | 22          | 1.511              | 22          | 1.666              | 24          | 1.703              | 22          | 2.21              |



where R532nm, T638nm, T405nm and R650nm stand for, respectively, spectral images in reflection mode at 532 nm, transmission mode at 638 nm, transmission mode at 405 nm and reflection mode at 650 nm.

Figure 5 shows the image acquired using the transmission mode with a laser at 405 nm as an example to illustrate the full field of view. The same region of interest is acquired for transmission mode with a laser at 638 nm, and reflection mode with lasers at 532 nm and 650 nm. In order to better compare the effectiveness of the MIs relative to the various spectral modes and laser wavelengths, we applied the proposed contrast functions to a cropped region of interest and the same area (Figure 8b) has been selected for the four images. The four corresponding selected areas are shown in Figure 8.

The histogram shows two separated Gaussian-like peaks. The first represents the red blood cells and the second for the image background which is the blood plasma. Both are mainly composed of haemoglobin. However, because of the packed and higher concentration of haemoglobin within erythrocytes and their thickness, the transmittance is weaker. The narrow-band histogram and separated peak shapes is explained by the use of a narrower illumination bandwidth, and enables a more effective image segmentation approach for red blood cell selection and counting. Figure 7 shows the

result using a simple threshold operation technique with a value of 0.48 located between the two peaks of the histogram plot.

Figures 8a, 8b, 8c and 8d correspond, respectively, to the Malaria Infection Indices MII1, MII2, MII3 and MII4.

The selected area shows, from a visual inspection, at least three possible infected red blood cells. The image in Figure 8a shows no evidence of parasitised erythrocyte. Unlike Figure 8a, Figures 8b, 8c and 8d confirm the presence of three infected red blood cells; Figures 8b and 8d show three dark spots within three erythrocytes and Figure 8c displays three bright spots (shown with red arrows). These spots show that the homogeneity of the erythrocytes is affected by a local reduction of the haemoglobin concentration due to their ingestion by the parasite.<sup>12,31</sup>

The blood smear is mainly composed of haemoglobin and the highest absorption peak is at about 405 nm. In addition, the absorption band of hemozoin,<sup>32</sup> which is the malaria parasite digestion by-product, is expected around 650 nm. The parasite activities are characterised by the ingestion of haemoglobin in the parasite food vacuole and its digestion, leading to a reduction of the haemoglobin concentration within the erythrocytes. The second malaria detection target is more sensitive because it can be seen at the very early

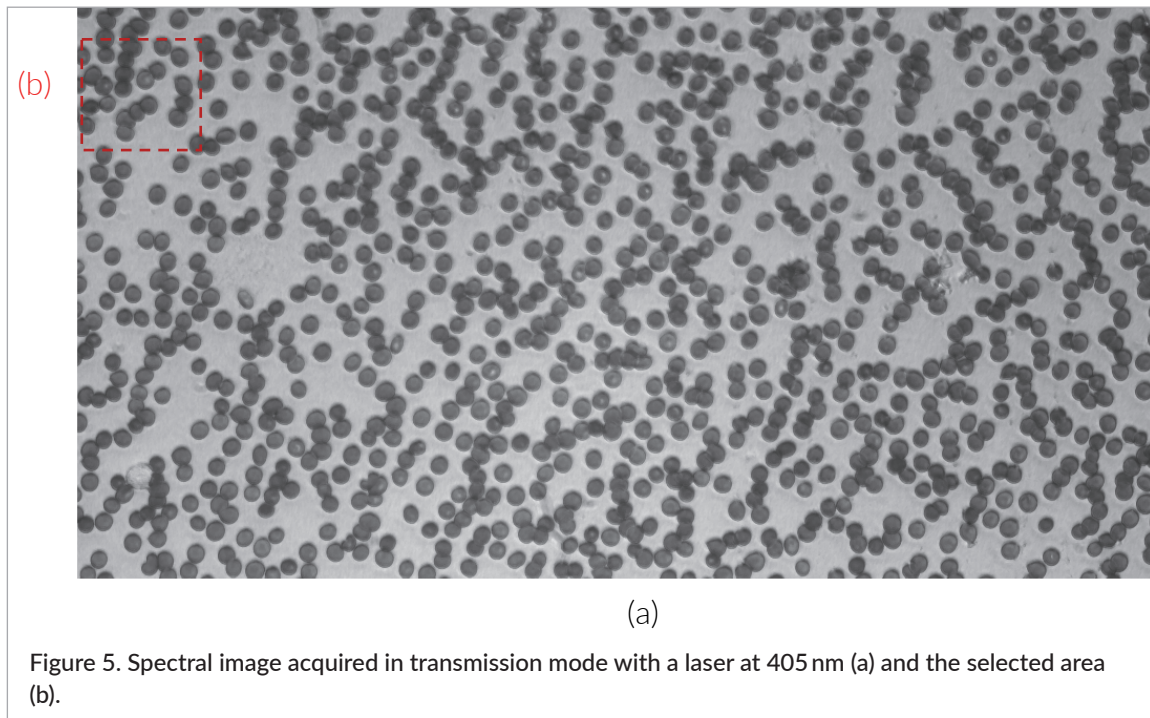


Figure 5. Spectral image acquired in transmission mode with a laser at 405 nm (a) and the selected area (b).

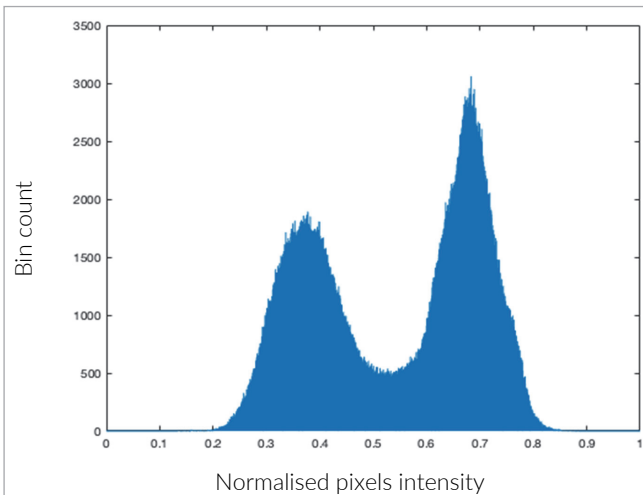


Figure 6. Histogram plot of the transmission mode image for the 405 nm laser.

infection stage. The hemozoin target is appropriate for later stages. Both 405 nm and 650 nm are, therefore, ideal wavelengths to derive a contrast function which can be described as a MII. The best contrast images resulting from the proposed MII are thus expected to be obtained from equations related to these two wavelengths, as opposed to the lasers at 532 nm and 638 nm. MII1 and MII3 exploit the contrast given by the absorption, and MII2 and MII4 are related to transmittance as the absorbance is obtained by applying log function to the transmittance. Since the transmittance and absorbance coefficients are inversely related, the resulting images exhibit inverse contrasts. The

transmittance contrast is higher than the absorbance one because of the application of the log function. The spots within the red blood cells account for the reduction of the haemoglobin presence due to its digestion by the parasites in these regions.

Figure 9 is a comparison of the same ROI for MII4 and fluorescence images. The fluorescence image is acquired with a laser at 405 nm with a high pass band edge filter at 450 nm.

The low contrast of Figure 9b is due to lower fluorescence efficiency compared to the transmittance image. The fluorescence image is shifted to the left due to chromatic aberration. The haemoglobin concentration decreasing within the erythrocyte is seen as lighter pixels.

We were not able to distinguish the infected and healthy erythrocytes with polarisation microscopy with this specific ROI because of the early infection stage of these cells. Therefore, we selected another ROI with a later stage of infection in order to detect the parasite by-product which is capable of exhibiting birefringence properties. Results are shown in Figure 10.

Figure 10a is a greyscale representation of the blood smear ROI with the parasite by-product hemozoin within the cell. For a better visual inspection, we have also presented the same image with another colour map representation. In Figure 10b the yellow spot, which appears white in Figure 10a, accounts for hemozoin. The parasite by-product commonly suggests a late stage of the infection and exhibits birefringent properties which can be detected under polarisation configuration.

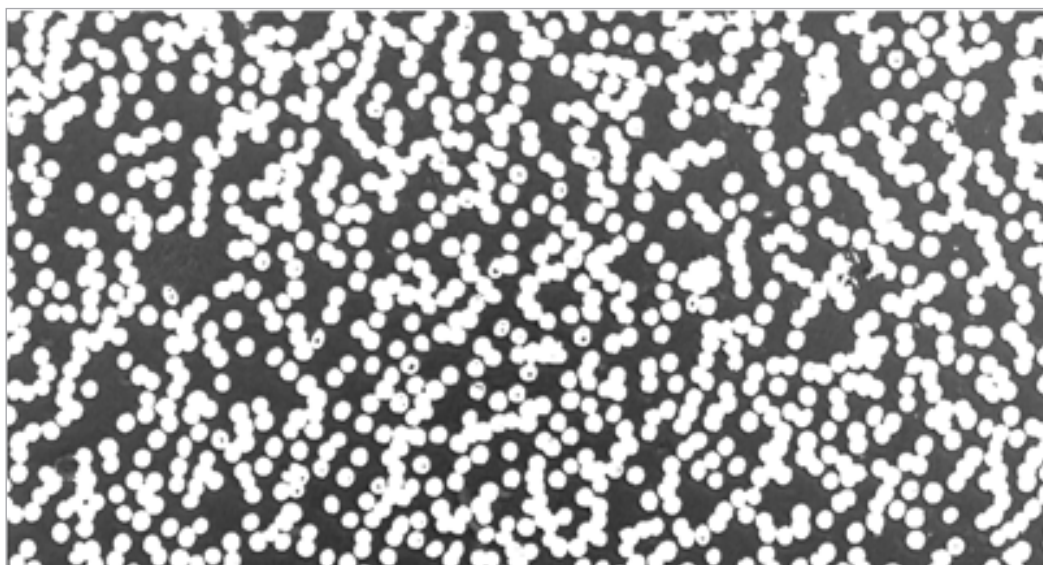


Figure 7. Segmented red blood cells image.

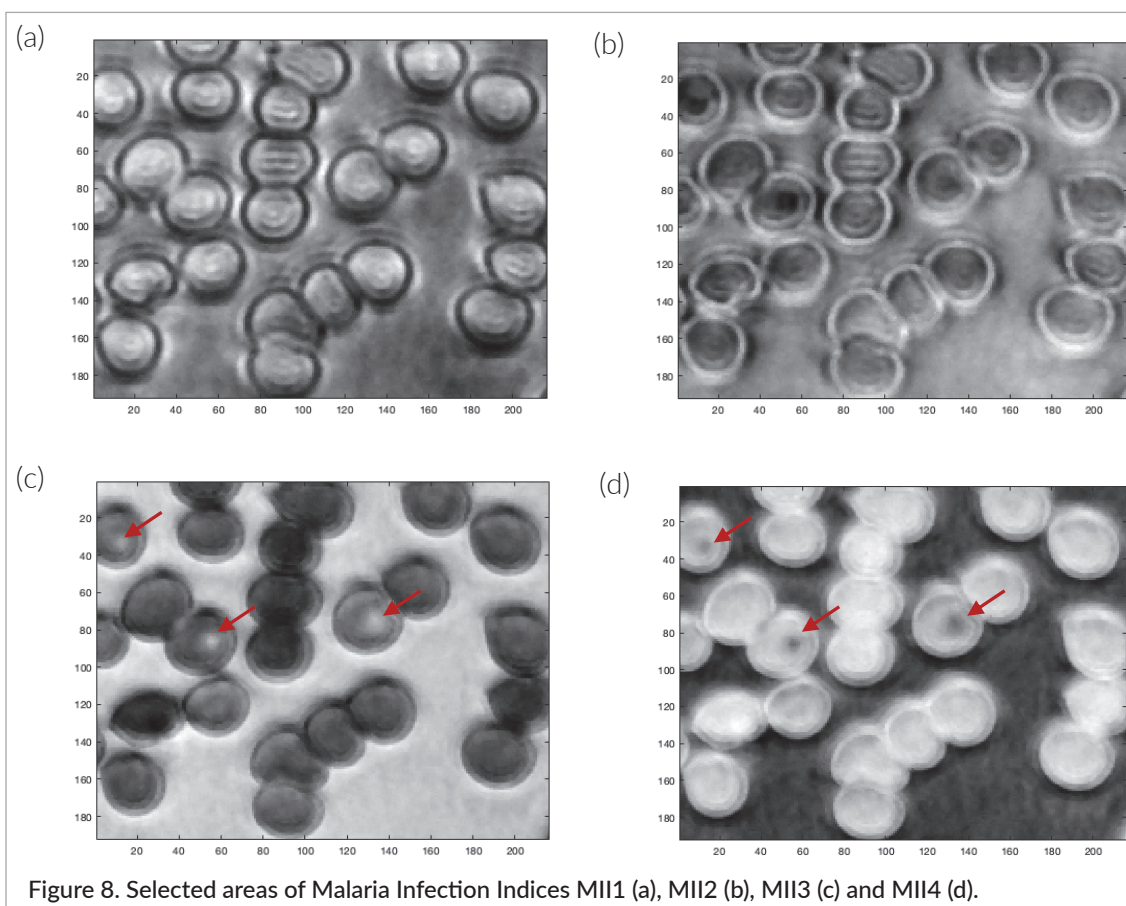


Figure 8. Selected areas of Malaria Infection Indices MII1 (a), MII2 (b), MII3 (c) and MII4 (d).

## Conclusion

We have designed and built a new and versatile research optical microscope based on laser illumination. Despite its flexibility and multi-purpose design, the initial objective of this microscope is to improve the detection and differentiation of healthy and infected blood cells. The

use of a narrower illumination bandwidth has permitted us to propose an efficient Malaria Infection Index which has shown the capability to detect malaria infection earlier. Fluorescence and polarisation modalities have also demonstrated that both earlier and later malaria infection detection can be improved using the upgraded system.<sup>24,32-38</sup> We have equipped the system with an

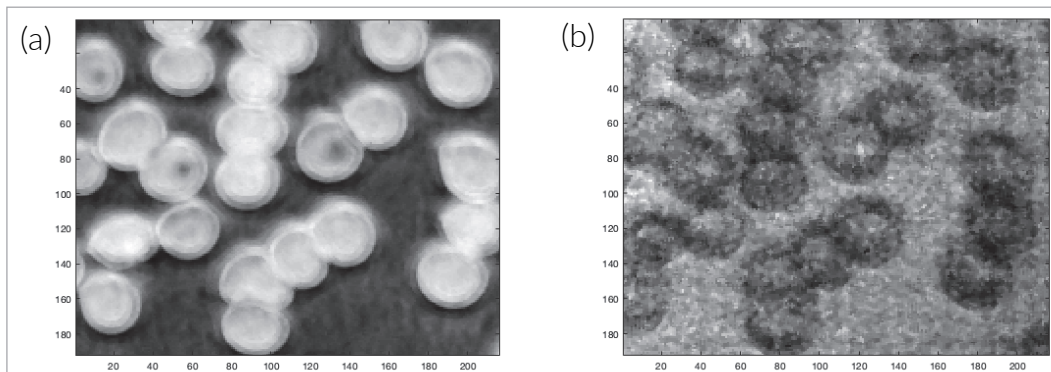


Figure 9. Comparison between MII4 of Equation (14) (a) and fluorescence (b) images.

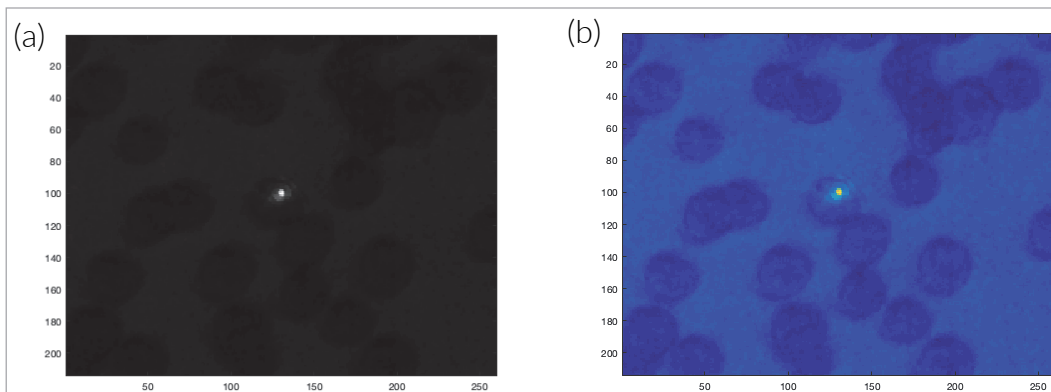


Figure 10. Comparison between greyscale (a) and colour (b) maps representation of the polarisation blood smear image.

autofocus algorithm for finding the best in-focus. The capability of the system to accept new microscope configurations has improved the robustness and effectiveness of the malaria detection procedure. This has been possible by using fewer illumination sources than in our previous work<sup>10-14</sup> to highlight malaria-infected red blood cells.

Moreover, the developed system is an improvement on standard microscopes, including the multispectral microscope-based LEDs, with the use of laser lights as illumination sources. Compared to LEDs, laser illumination presents many advantages, such as improved image brightness, power efficiency, sample content-specific spectral footprints and image contrast which is very useful in differentiating the objects in an image.<sup>25,26</sup> However, it does have limitations such as speckle noise. The built system is capable of performing defocus, autofocus, field scanning and coordinates backup. It is fully controlled by an application through which the focal plane setting is performed using a second-derivative-based algorithm.

## Acknowledgements

Sida (the Swedish International Development Cooperation Agency) through ISP (the International Science Programme, Uppsala University) is acknowledged for financial support during the building of the system. Aboma Merdasa and Edouard Berrocal from Lund University (Sweden) are also acknowledged for their technical support.

## References

1. D.J. Brady, *Optical Imaging and Spectroscopy*. John Wiley & Sons (2009). <https://doi.org/10.1002/9780470443736>
2. A.S. Stender, K. Marchuk, C. Liu, S. Sander, M.W. Meyer, E.A. Smith, B. Neupane, G. Wang, J. Li, J.-X. Cheng, B. Huang and N. Fang, "Single cell optical imaging and spectroscopy", *Chem. Rev.* **113**(4), 2469–2527 (2013). <https://doi.org/10.1021/cr300336e>

3. W.E. Moerner, M. Orrit, U.P. Wild and T. Basché (Eds), *Single-Molecule Optical Detection, Imaging and Spectroscopy*. John Wiley & Sons (2008).
4. R. Shrestha, J.Y. Hardeberg and G.U. College, "Multispectral imaging using LED illumination and an RGB camera", *21st Color and Imaging Conference*. Society for Imaging Science & Technology, pp. 8–13 (2013).
5. N.L. Everdell, I.B. Styles, A. Calcagni, J. Gibson, J. Hebden and E. Claridge, "Multispectral imaging of the ocular fundus using light emitting diode illumination", *Rev. Sci. Instrum.* **81(9)**, 093706 (2010). <https://doi.org/10.1063/1.3478001>
6. R.M. Levenson and J.R. Mansfield, "Multispectral imaging in biology and medicine: slices of life", *Cytometry A* **69(8)**, 748–758 (2006). <https://doi.org/10.1002/cyto.a.20319>
7. G.C. Holst and T.S. Lomheim, *CMOS/CCD Sensors and Camera Systems*. SPIE (2007).
8. E.F. Schubert, *Light-Emitting Diodes* (2nd Edn). Cambridge University Press (2006). <https://doi.org/10.1017/CBO9780511790546>
9. K. Petermann, *Laser Diode Modulation and Noise* (Vol. 3). Springer (2012).
10. J.T. Zoueu, S. Ouattara, A. Toure, S. Safi and S.T. Zan, "Spectroscopic approach of multispectral imaging of *Plasmodium falciparum*-infected human erythrocytes", *2009 3rd ICTON Mediterranean Winter Conference (ICTON-MW)*, Angers, pp. 1–7 (2009). <https://doi.org/10.1109/ICTONMW.2009.5385598>
11. M. Brydegaard, A. Merdasa, H. Jayaweera, J. Ålebring and S. Svanberg, "Versatile multispectral microscope based on light emitting diodes", *Rev. Sci. Instrum.* **82(12)**, 123106 (2011). <https://doi.org/10.1063/1.3660810>
12. J.T. Zoueu and S.G.T. Zan, "Trophozoite stage infected erythrocyte contents analysis by use of spectral imaging LED microscope", *J. Microsc.* **245(1)**, 90–99 (2012). <https://doi.org/10.1111/j.1365-2818.2011.03548.x>
13. O.K. Bagui, J.T. Zoueu and C. Wählby, "Automatic malaria diagnosis by the use of multispectral contrast imaging", *Phys. Chem. News* **75**, 86–98 (2015).
14. A. Merdasa, M. Brydegaard, S. Svanberg and J.T. Zoueu, "Staining-free malaria diagnostics by multispectral and multimodality light-emitting-diode microscopy", *J. Biomed. Optics* **18(3)**, 036002 (2013). <https://doi.org/10.1117/1.JBO.18.3.036002>
15. M. Sangare, C. Tekete, O.K. Bagui, A. Ba and J.T. Zoueu, "Identification of bacterial diseases in rice plants leaves by the use of spectroscopic imaging", *Appl. Phys. Res.* **7(6)**, 61 (2015). <https://doi.org/10.5539/apr.v7n6p61>
16. A.K. Kouakou, O.K. Bagui, T.A. Agneroh, A.P. Soro and J.T. Zoueu, "Cucumber mosaic virus detection by artificial neural network using multispectral and multimodal imagery", *Optik* **127(23)**, 11250–11257 (2016). <https://doi.org/10.1016/j.ijleo.2016.09.035>
17. A.K. Kouakou, A.P. Soro, A.K. Taky and J.T. Zoueu, "Multi-spectral and fluorescence imaging in prevention of overdose of herbicides: the case of maize", *Spectral Anal. Rev.* **5(2)**, 11–24 (2017). <https://doi.org/10.4236/sar.2017.52002>
18. P. Török and F.J. Kao, *Optical Imaging and Microscopy: Techniques and Advanced Systems*. Springer (2007).
19. A. Chaddad, C. Desrosiers, L. Hassan and M. Toews, "Multispectral texture analysis of histopathological abnormalities in colorectal tissues", *2016 IEEE International Conference on Image Processing (ICIP)*, Phoenix, AZ, pp. 2628–2632 (2016). <https://doi.org/10.1109/ICIP.2016.7532835>
20. R. Peyret, A. Bouridane, S.A. Al-Maadeed, S. Kunhoth and F. Khelifi, "Texture analysis for colorectal tumour biopsies using multispectral imagery", *2015 37th Annual International Conference of the IEEE Engineering in Medicine and Biology Society (EMBC)*, Milan, pp. 7218–7221 (2015). <https://doi.org/10.1109/EMBC.2015.7320057>
21. F.B. Tek, A.G. Dempster and I. Kale, "Computer vision for microscopy diagnosis of malaria", *Malaria J.* **8(1)**, 153 (2009). <https://doi.org/10.1186/1475-2875-8-153>
22. M. Agnero, K. Konan, A. Kossonou, O. Bagui, J. Zoueu, M.A. Agnero and J.T. Zoueu, "A new method to retrieve the three-dimensional refractive index and specimen size using the transport intensity equation, taking diffraction into account", *Appl. Sci.* **8(9)**, 1649 (2018). <https://doi.org/10.3390/app8091649>
23. T.A. Klar, S. Jakobs, M. Dyba, A. Egner and S.W. Hell, "Fluorescence microscopy with diffraction resolution barrier broken by stimulated emission", *Proc. Nat. Acad. Sci.* **97(15)**, 8206–8210 (2000). <https://doi.org/10.1073/pnas.97.15.8206>
24. M. Wolman, "Polarized light microscopy as a tool of diagnostic pathology", *J. Histochem. Cytochem.* **23(1)**, 21–50 (1975). <https://doi.org/10.1177/23.1.1090645>
25. F.P. Shevlin, "Speckle reduction in laser-illuminated picoprojectors", *Proceedings Volume 8252, MOEMS*

- and Miniaturized Systems XI, p. 825206 (2012). <https://doi.org/10.1117/12.912805>
26. J. Opoku-Ansah, M.J. Eghan, B. Anderson, J.N. Boampong and P.K. Buah-Bassuah, "Laser-induced autofluorescence technique for *Plasmodium falciparum* parasite density estimation", *Appl. Phys. Res.* **8(2)**, 43 (2016). <https://doi.org/10.5539/apr.v8n2p43>
  27. D. Lenz, P.G. Kreamsner, B. Lell, B. Biallas, M. Boettcher, B. Mordmüller and A.A. Adegnika, "Assessment of LED fluorescence microscopy for the diagnosis of *Plasmodium falciparum* infections in Gabon", *Malaria J.* **10(1)**, 194 (2011). <https://doi.org/10.1186/1475-2875-10-194>
  28. C. Buschmann, G. Langsdorf and H.K. Lichtenthaler, "Imaging of the blue, green, and red fluorescence emission plants: an overview", *Photosynthetica* **38(4)**, 483–491 (2000). <https://doi.org/10.1023/A:1012440903014>
  29. M. Alonso Bueno-Ibarra, J. Álvarez-Borrego, L. Acho and M. Cristina Chávez-Sánchez, "Fast autofocus algorithm for automated microscopes", *Opt. Eng.* **44(6)**, 063601 (2005). <https://doi.org/10.1117/1.1925119>
  30. D.L. Omucheni, K.A. Kaduki, W.D. Bulimo and H.K. Angeyo, "Application of principal component analysis to multispectral-multimodal optical image analysis for malaria diagnostics", *Malaria J.* **13**, 485 (2014). <https://doi.org/10.1186/1475-2875-13-485>
  31. G.A. Jamjoom, "Dark-field microscopy for detection of malaria in unstained blood films", *J. Clin. Microbiol.* **17(5)**, 717–721 (1983). <https://doi.org/10.1128/JCM.17.5.717-721.1981>
  32. Y. Serebrennikova, J. Patel and L. Garcia-Rubio, "Interpretation of the ultraviolet-visible spectra of malaria parasite *Plasmodium falciparum*", *Appl. Opt.* **49**, 180–188 (2010). <https://doi.org/10.1364/AO.49.000180>
  33. R.J. Maude, W. Buapetch and K. Silamut, "A simplified, low-cost method for polarized light microscopy", *Am. J. Trop. Med. Hygiene* **81(5)**, 782–783 (2009). <https://doi.org/10.4269/ajtmh.2009.09-0383>
  34. C.S. Scott, D. Zyl, E. Ho, D. Meyersfeld, L. Ruivo, B.V. Mendelow and T.L. Coetzer, "Automated detection of malaria-associated intraleucocytic haemozoin by Cell-Dyn CD4000 depolarization analysis", *Int. J. Lab. Hematol.* **25(2)**, 77–86 (2003). <https://doi.org/10.1046/j.1365-2257.2003.00496.x>
  35. C. Lawrence and J.A. Olson, "Birefringent hemozoin identifies malaria", *Am. J. Clin. Pathol.* **86(3)**, 360–363 (1986). <https://doi.org/10.1093/ajcp/86.3.360>
  36. D. Lenz, P.G. Kreamsner, B. Lell, B. Biallas, M. Boettcher, B. Mordmüller and A.A. Adegnika, "Assessment of LED fluorescence microscopy for the diagnosis of *Plasmodium falciparum* infections in Gabon", *Malaria J.* **10(1)**, 194 (2011). <https://doi.org/10.1186/1475-2875-10-194>
  37. P.C. Wever, Y.M.C. Henskens, P.A. Kager, J. Dankert and T. van Gool, "Detection of imported malaria with the Cell-Dyn 4000 hematology analyzer", *J. Clin. Microbiol.* **40(12)**, 4729–4731 (2002). <https://doi.org/10.1128/JCM.40.12.4729-4731.2002>
  38. F. Kawamoto, "Rapid diagnosis of malaria by fluorescence microscopy with light microscope and interference filter", *Lancet* **337(8735)**, 200–202 (1991). [https://doi.org/10.1016/0140-6736\(91\)92159-Y](https://doi.org/10.1016/0140-6736(91)92159-Y)